small methods
www.small-methods.com

An Integrated Microcurrent Delivery System Facilitates Human Parathyroid Hormone Delivery for Enhancing Osteoanabolic Effect

Xiaoyi Mo, Keyu Meng, Zehui Li, Shanwei Lan, Zhengda Ren, Xihong Fu, Chenglin Li, Tiancheng Sun, Denghui Xie, Zhongmin Zhang,* and Hui-Jiuan Chen**

Human parathyroid hormone (1–34) (PTH) exhibits osteoanabolic and osteocatabolic effects, with shorter plasma exposure times favoring bone formation. Subcutaneous injection (SCI) is the conventional delivery route for PTH but faces low delivery efficiency due to limited passive diffusion and the obstruction of the vascular endothelial barrier, leading to prolonged drug exposure times and reduced osteoanabolic effects. In this work, a microcurrent delivery system (MDS) based on multimicrochannel microneedle arrays (MMAs) is proposed, achieving high efficiency and safety for PTH transdermal delivery. The internal microchannels of the MMAs are fabricated using high-precision 3D printing technology, providing a concentrated and safe electric field that not only accelerates the movement of PTH but also reversibly increases vascular endothelial permeability by regulating the actin cytoskeleton and interendothelial junctions through Ca^{2+}-dependent cAMP signaling, ultimately promoting PTH absorption and shortening exposure times. The MDS enhances the osteoanabolic effect of PTH in an osteoporosis model by inhibiting osteoclast differentiation on the bone surface compared to SCI. Moreover, histopathological analysis of the skin and organs demonstrated the good safety of PTH delivered by MDS in vivo. In addition to PTH, the MDS shows broad prospects for the high-efficiency transdermal delivery of macromolecular drugs.

1. Introduction

Osteoporosis (OP) is characterized by reduced bone mass, damage to bone microstructure, and compromised strength, which render elderly individuals vulnerable to low-energy fractures.[1] Although osteoanabolic drugs are more effective than anti-osteocatabolic drugs in promoting bone formation, their ability to increase hip bone mineral density (BMD) is limited to approximately 5%,[2] which is insufficient to meet the needs of middle-aged and elderly patients with severe OP for long-term bone health. As the longest-used and most clinically evidenced osteoanabolic drug, human parathyroid hormone (1–34) (PTH) also has a catabolic effect that promotes bone resorption.[3] Previous studies have attempted to weaken or eliminate the osteocatabolic action of PTH while maintaining its osteoanabolic effect to generate a more potent osteogenic ability,[4] but only limited progress has been achieved to date.

Exposure time, rather than C_{max}, is crucial to the mechanism of PTH's anabolic action.[5] Exposure time is defined as the duration from appearance in plasma until complete elimination. The exposure time of PTH subcutaneous injection (SCI) is prolonged due to the obstruction of the vascular endothelial barrier and the molecular weight of PTH (4117.77 Da), leading to sustained enhancement of osteoclast differentiation even after

X. Mo, K. Meng, Z. Li, S. Lan, Z. Ren, Z. Zhang
Division of Spine Surgery
Department of Orthopaedics
Nanfang Hospital
Southern Medical University
Guangzhou 510515, China
E-mail: zzmzzc@smu.edu.cn

The ORCID identification number(s) for the author(s) of this article can be found under https://doi.org/10.1002/smtd.202401144

DOI: 10.1002/smtd.202401144

X. Fu
Institute of Precision Medicine
The First Affiliated Hospital of Sun Yat-sen University
Guangzhou 510080, China

C. Li, T. Sun, H.-J. Chen
State Key Laboratory of Optoelectronic Materials and Technologies
Province Key Laboratory of Display Material and Technology
School of Electronics and Information Technology
Sun Yat-Sen University
Guangzhou 510006, China
E-mail: chenhuix5@mail.sysu.edu.cn

D. Xie
Department of Orthopedic Surgery
Center for Orthopedic Surgery
The Third Affiliated Hospital of Southern Medical University
Guangzhou 510630, China
E-mail: xiedenghui221122@smu.edu.cn

maximal osteogenic induction is achieved.[6–8] Although many studies have attempted to explore PTH analogues with shorter plasma exposure times, limited effects have been achieved.[9,10]

PTH is a positively charged peptide when dissolved at physiological pH due to the presence of multiple basic amino acid residues, such as lysine and arginine.[11] Therefore, an electric field, in the form of electroporation or microcurrent, can provide an additional electro-driving force to accelerate the movement of PTH in subcutaneous interstitial fluid. Furthermore, electroporation and microcurrent have been proposed to increase vascular endothelial permeability,[12,13] which is thought to facilitate the transendothelial transport of subcutaneous PTH. These synergistic effects can promote the absorption rate of subcutaneous PTH and reduce exposure time. The endothelial barrier, formed by lateral connections at cell–cell junctions, is a critical factor in determining vascular permeability.[14] Central to the regulation of the endothelial barrier is transmembrane adhesion proteins, whose backbone of VE-cadherin anchoring together with the actin cytoskeleton forms the barrier interface.[15] Various extracellular stimuli, including electro-stimulation, can modulate barrier function by altering VE-cadherin and the cytoskeleton, with Ca^{2+} signaling playing a vital role. Increased intracellular Ca^{2+} triggers various signaling pathways, including RhoA (Ras homolog family member A) and its downstream effector ROCK (Rho-associated protein kinase), which promote actin stress fibers (SFs) contraction, thereby disrupting VE-cadherin and resulting in decreased stability of the endothelial barrier.[16] The biosafety of electro-stimulation is critical for the endothelial barrier due to the long-term and repeated administration of PTH, requiring the insult to be sufficiently mild to prevent cell necrosis. Electroporation usually causes extensive and irreversible disruption to the cell cytoskeleton.[17] Although microcurrents have been reported to reversibly increase endothelial permeability, these results were based on mathematical simulations, and the underlying mechanisms remain unclear.[18]

Transdermal delivery is superior to conventional SCI in terms of efficiency, convenience, and patient preference for osteoporotic osteoanabolic therapies.[19] Scholars have attempted to deliver PTH transdermally using microcurrents or high-voltage electroporation on the skin surface; however, due to the compact packing of the stratum corneum, neither increased drug dosage nor electric field intensity has achieved satisfactory results.[20,21] Physically breaking the barrier of the stratum corneum by creating microchannels in the epidermis is fundamental for ensuring effective transdermal drug delivery. Since most drug molecules are charged, an external electric field is typically employed to control the direction and speed of drug flow. Consequently, the use of microneedle (MN) arrays in combination with an external electric field has become a widely adopted strategy in the development of drug-delivery devices.[22] Numerous microcurrent-based MN systems (such as iontophoresis) have been proposed for transdermal drug delivery, including insulin and even macromolecular proteins.[23,24] Yuan Yang et al. incorporated conductive materials with a piezoelectric nanogenerator into microneedles, achieving self-powered and controlled transdermal administration of dexamethasone.[25] Furthermore, wearable devices based on MN technology have recently enabled in situ transdermal detection and delivery of methotrexate using iontophoresis.[26] However, previous reports have primarily focused on optimizing the electro-driving force of microcurrents to improve the efficiency and convenience of transdermal delivery, while neglecting the potential effects and safety of microcurrents on subcutaneous blood vessels.

Herein, we present an integrated microcurrent delivery system (MDS) for PTH transdermal delivery. The MDS demonstrates excellent biocompatibility and high efficiency for PTH delivery, ultimately enhancing the osteoanabolic effect of PTH by reducing PTH exposure time compared to SCI. Considering cost-effectiveness and flexibility, the through-microchannels were constructed using high-precision 3D printing technology in multimicrochannel microneedle arrays (MMAs).[27] The syringe positive electrode of MDS pushes the drug solution into the subcutaneous interstitial fluid, forming a complete circuit between the positive electrode, the drug solution, the subcutaneous interstitial fluid, and the negative electrode, which drives positively charged drug molecules, such as PTH, to move from the positive electrode toward the negative electrode (Figure S1, Supporting Information). The non-conductive property of the MMAs concentrates the electric field for dual functions: 1) accelerating the movement of charged PTH in subcutaneous interstitial fluid; 2) concentrating low and safe microcurrents that regulate the cytoskeleton and VE-cadherin via the Ca^{2+}/cAMP pathway, causing a reversible increase in endothelial permeability and promoting PTH absorption. To prove the clinical value of the MDS for PTH delivery, we first confirmed that it improves delivery efficiency and shortens exposure time compared to SCI both in vitro and in vivo. Furthermore, using OP rat models, we demonstrated that PTH delivered by the MDS significantly enhanced the osteoanabolic effect by inhibiting osteoclast differentiation compared to SCI. Beyond PTH, the proposed MDS shows great promise for the high-efficiency transdermal delivery of macromolecular drugs (**Figure 1**).

2. Results and Discussion

2.1. Design and Fabrication of the Microcurrent Delivery System (MDS)

MDS is designed to integrate microcurrent for subcutaneous drug delivery and consists of MMAs, a syringe positive electrode, counter electrode microneedles (MNs) as the negative electrode, and an injection cap (**Figure 2A**). Since PTH is clinically administered via a syringe, a silver layer is sputtered onto the flattened rubber end of the syringe pusher to serve as the positive electrode, which is then connected to the external power source through a silver wire. The counter electrode MNs, functioning as the negative electrode, are combined with the positive electrode through a matching injection cap (Figure 2B–F). The counter-electrode MNs have a base diameter of approximately 40 µm, a length of approximately 100 µm, and a spacing of approximately 110 µm between adjacent MNs. The counter-electrode MNs are then sputtered with a ≈100 nm Au layer to ensure excellent biocompatibility, as validated in our previous studies.[28]

MMAs were fabricated using high-resolution 3D printing technology with biocompatible photosensitive resin (Figure 2G; Figure S2, Supporting Information). The high precision and flexibility of this technology allow for customization of MN size, array density, and microchannel diameter to suit the delivery

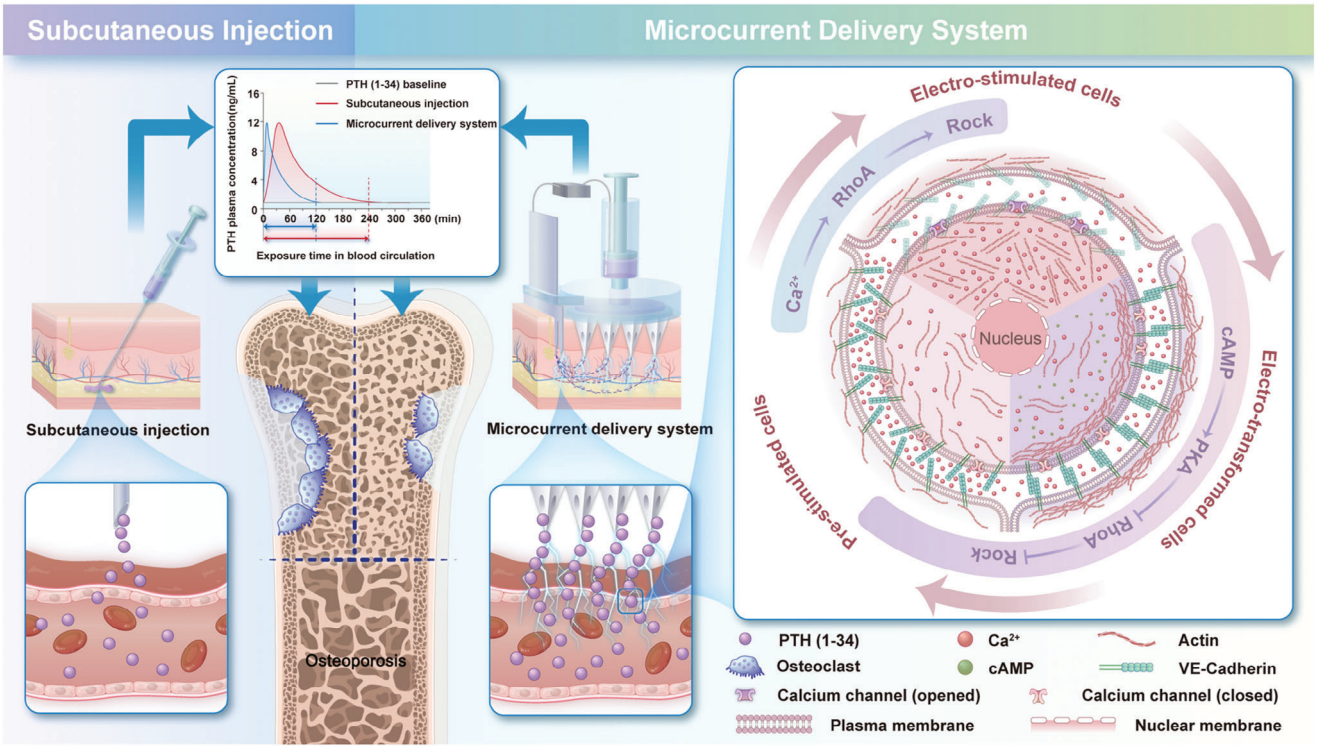

Figure 1. Schematic diagram of MDS improving the osteoanabolic effect of PTH compared to subcutaneous injection and the Ca^{2+}-dependent cAMP signaling mechanism.

requirements of different drugs. The MMAs manufactured in this study have a base diameter of 8 mm, with 4 × 4 MNs positioned at the center of the base, spaced 800 µm from center to center. Each pyramidal MN has a base length of 600 µm and a height of 850 µm, with an average edge length of the tip measuring 18.2 ± 2.4 µm (Figure S3, Supporting Information). Each of the four sides of the pyramidal MN features a through-microchannel with a 100 µm diameter for drug transport, as visualized by SEM micrographs (Figure 2H–J). The square base of the pyramidal MN has been shown to withstand higher axial and transverse forces compared to a circular base.[29] The MN tip was designed as a solid structure with microchannels open on the sides to ensure the mechanical stability of the MMAs for penetrating skin tissue and reducing reverse diffusion.[30]

The MMAs contain multiple through-microchannels to ensure the high delivery efficiency of the MDS. Since the MMAs are made of non-conductive resin, when the MMAs and the counter electrode MNs penetrate the skin and contact the interstitial fluid, a complete circuit is established between the positive electrode, the drug solution, the subcutaneous interstitial fluid, and the negative electrode. This configuration accelerates the movement of charged molecules (e.g., positively charged PTH).

2.2. Determination of the Optimum Microcurrent and the Diameter of Microchannels

Since PTH requires daily delivery, the biocompatibility of microcurrent is particularly important for the MDS. MDS combined with different microcurrent densities was used to explore their effects on the biocompatibility of human umbilical vein endothelial cells (HUVECs) in vitro. The live/dead staining results showed that a microcurrent density of 1 mA cm^{-2} for 5 min exhibited excellent biocompatibility, while a significant percentage of dead cells appeared at 2 mA cm^{-2} (Figure S4A,B, Supporting Information). Further assessment using the CCK-8 assay revealed that a microcurrent density of 2 mA cm^{-2} for 5 min significantly inhibited cell proliferation, whereas a microcurrent density of 1 mA cm^{-2} for 5 min demonstrated good proliferation safety at 1 and 3 days (Figure S4C, Supporting Information). Given that HUVEC proliferation also declined with longer stimulation times (>7 min) at 1 mA cm^{-2} (Figure S4D, Supporting Information), we employed 7-min stimulation periods in the remaining experiments to achieve optimal delivery effects while maximizing cell viability.

A simulation model of the MDS was established to explore the optimal diameter of microchannels. The simulated results demonstrated that the microchannel diameter was related to the applied voltage, the flow rate of the drug, and the mechanical stability under a microcurrent of 1 mA cm^{-2} (Figure S5A–C, Supporting Information). The diameter-related simulation curves indicated that diameters of 100, 140, or 180 µm might be optimal for the microchannels of MMAs (Figure S5D, Supporting Information). However, the mechanical properties, as a fundamental factor for penetrating skin tissue, need further verification.[31] The vertical deformations of MMAs with microchannel diameters of 100, 140, and 180 µm were observed under a compressive force increasing from 0 to 20 N (Figure S6A–I, Supporting

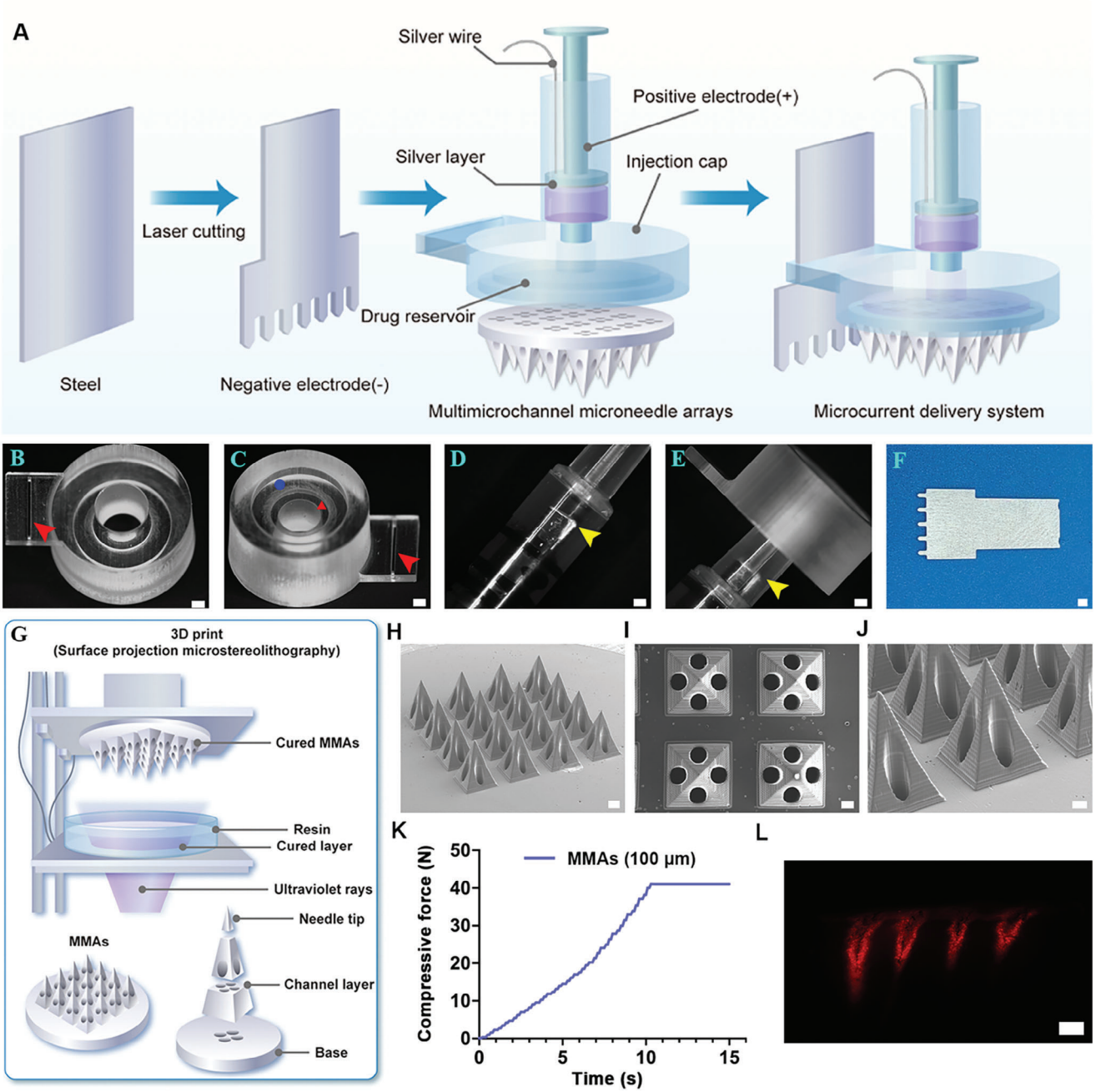

Figure 2. Design and characterization of the MDS. A) Components of the MDS. The counter electrode MNs and the pusher head of the syringe act as the negative and the positive electrode, respectively. The negative electrode, the positive electrode and the MMAs are loaded into the injection cap together to assemble the MDS. B,C) Optical micrographs showing the top view (B) and the bottom view (C) of the injection cap. The red arrows and the blue circle represent the rectangular groove for loading counter electrode MNs and the circular groove for loading MMAs, respectively. The red triangle represents the drug reservoir. Scale bar, 1000 μm. D,E) The silver layer and the silver wire (yellow arrows) at the end of the syringe pusher as the positive electrode, and the head of syringe can be fitted into the injection cap. F) Optical image of the counter electrode MNs. Scale bar, 100 μm. G) Schematic diagram of the 3D-print process of the MMAs (top), and the layer-by-layer structure of the MMAs shows the internal microchannels through the base and the inside of MNs (bottom). H,I) Representative side view and top view of MMAs. Scale bar, 100 μm. J) Representative image of a single MN. Scale bar, 100 μm. K) Mechanical curve of MMAs with microchannels of 100 μm diameter under compressive force. L) Rhodamine B staining of MMAs penetration wounds in porcine skin. Scale bar, 200 μm.

Information). The tips of the MMAs with a microchannel diameter of 140 µm were severely deformed, and those with a diameter of 180 µm experienced significant collapse. Therefore, MMAs with a microchannel diameter of 100 µm were selected for subsequent verification. The force–time curve demonstrated that MMAs with a microchannel diameter of 100 µm did not reach the fracture point when the compressive force was increased from 0 to 40 N (Figure 2K), indicating high mechanical properties that meet clinical needs.[32] According to previous reports, the force required to insert into the skin ranges from 0.08 to 3.04 N,[33] so our MMAs are fully capable of puncturing the skin. Pig skin was used to verify the penetration ability of the MMAs, and the needle-shaped outline stained with rhodamine B indicated successful skin piercing (Figure 2L).

2.3. MDS Reversibly Increased Endothelial Permeability In Vitro

HUVEC monolayers were established to explore the effect of MDS with different microcurrent densities (7 min) on endothelial permeability. The results of the transendothelial electrical resistance (TEER) indicated that the disruption of monolayer integrity was positively correlated with microcurrent density (**Figure 3A**). Conversely mirroring the transient changes in TEER values, the endothelial permeability of HUVEC monolayers to fluorescein isothiocyanate-labeled dextran (FITC-dextran, 5 kDa, PTH analog) increased with rising microcurrent densities (Figure 3B). To further understand the dynamic effect on endothelial permeability triggered by the optimal delivery parameters for maximizing cell viability (7 min at 1 mA cm^{-2}), it was found that TEER values decreased first following microcurrent stimulation, then increased spontaneously and finally returned to baseline. The transient changes in endothelial permeability exhibited an inverse relationship with the TEER values (Figure 3C,D), indicating a rapid and spontaneous recovery of endothelial permeability.

RNA sequencing was applied to reveal the mechanism of spontaneous recovery of endothelial permeability in MDS-stimulated (7 min at 1 mA cm^{-2}) HUVEC monolayers. There were 618 upregulated genes and 279 downregulated genes following MDS stimulation (Figure S7A,B, Supporting Information). The downregulated genes were subjected to Kyoto Encyclopedia of Genes and Genomes (KEGG) pathway enrichment analysis, which showed that the regulation of the actin cytoskeleton was significantly enriched, with the highest gene ratio and the most significant p-value (Figure S7C,D, Supporting Information, Table S1). The actin cytoskeleton and VE-cadherin have been reported to be involved in the regulation of endothelial permeability induced by electrical stimulation.[34,35] We observed noticeable differences in the actin cytoskeleton 0.5 h after exposure to the MDS with different power settings (Figure 3E). Specifically, differences in actin fiber orientation and associated VE-cadherin were noted: at lower microcurrent densities (<1 mA cm^{-2}) and in control cells, the intracellular space was dominated by stressed fibers (SFs) and serrated VE-cadherin (SVE), while SFs and SVE were increasingly replaced by circumferential bundles (CBs) and smooth linear VE-cadherin (LVE) following exposure at 1 mA cm^{-2}. However, excessive contraction of SFs and destruction of VE-cadherin were observed at 2 mA cm^{-2} was confirmed by immunofluorescence analysis of intracellular actin and junctional regions where VE-cadherin and CBs are localized (Figure 3F,G). We also observed a significant increase in cell size and a corresponding decrease in the linearity index (the junction length/the distance between vertices) at 1 mA cm^{-2} (Figure 3H,I). An increased linearity index is typically associated with a decrease in the intercellular gap due to the tightening of the endothelial barrier.[36] At 2 mA cm^{-2}, VE-cadherin disappeared with the contraction of SFs, similar to the stressed cell state seen in pathological conditions such as trauma and inflammation.[37,38]

The dynamics of actin and VE-cadherin reconstruction triggered by MDS exposure (1 mA cm^{-2}) were further explored and can be summarized into three phases: 1) pre-stimulated cells (control): the cytoskeleton predominantly exists in the form of SFs and SVE; 2) electro-stimulated cells: within 0.1 h post-exposure, SVE and CBs were almost completely disintegrated, with an increase in intracellular actin leading to cell contraction, as evidenced by smaller cell size and reduced linearity; 3) electrotransformed cells: with cellular relaxation, SVE patterns gradually transform into stable LVE at 0.5 h post-exposure and intracellular SFs are progressively replaced by CBs, as indicated by the loss of fluorescence of intracellular actin. These changes are also indirectly observed through increasing cell sizes and the linearity index. After 4 h, SVE reappeared as the cells progressed from a challenged state toward recovery. The intracellular SFs and cell morphology relaxed back to their original pre-stimulated state 24 h post-exposure (Figure 3J–N). Long Lin et al. proposed a multimicrochannel microneedle microporation platform that efficiently delivers chemotherapy drugs locally into tumor cells through electroporation of the cell membrane, significantly enhancing the anti-tumor effect. However, this method is not suitable for regulating vascular endothelial cells to promote the absorption and circulation of PTH. Furthermore, the long-term use of electroporation may pose safety risks to endothelial cells. In contrast, our results indicate that the reversible increase in endothelial permeability induced by microcurrent might offer a safer alternative.[39]

2.4. Ca^{2+}-Dependent cAMP Mediates Reversible Increase of Endothelial Permeability via ROCK Activation and Inhibition

Figure 3 shows the spontaneous cytoskeleton remodeling following MDS stimulation. To date, no studies have investigated the dynamic rebalancing of actin and VE-cadherin triggered by electro-stimulation. Pulsed electric fields, in the form of electroporation, typically cause extensive and irreversible destruction of the cytoskeleton, leading to decreased cell viability,[40] which is unsuitable for long-term drug delivery. Additionally, previous studies on microcurrent-assisted MNs have primarily focused on the driving force provided by microcurrent, often overlooking its effect on vascular permeability.[41] To elucidate the spontaneous cytoskeleton remodeling of HUVEC monolayers triggered by MDS, we further investigated the underlying signaling mechanisms.

VE-cadherin consists of a long extracellular domain that mediates calcium-dependent cellular adhesion.[42] Previous studies have suggested that the interaction between electrical stimulation and the cytoskeleton mainly involves transient membrane

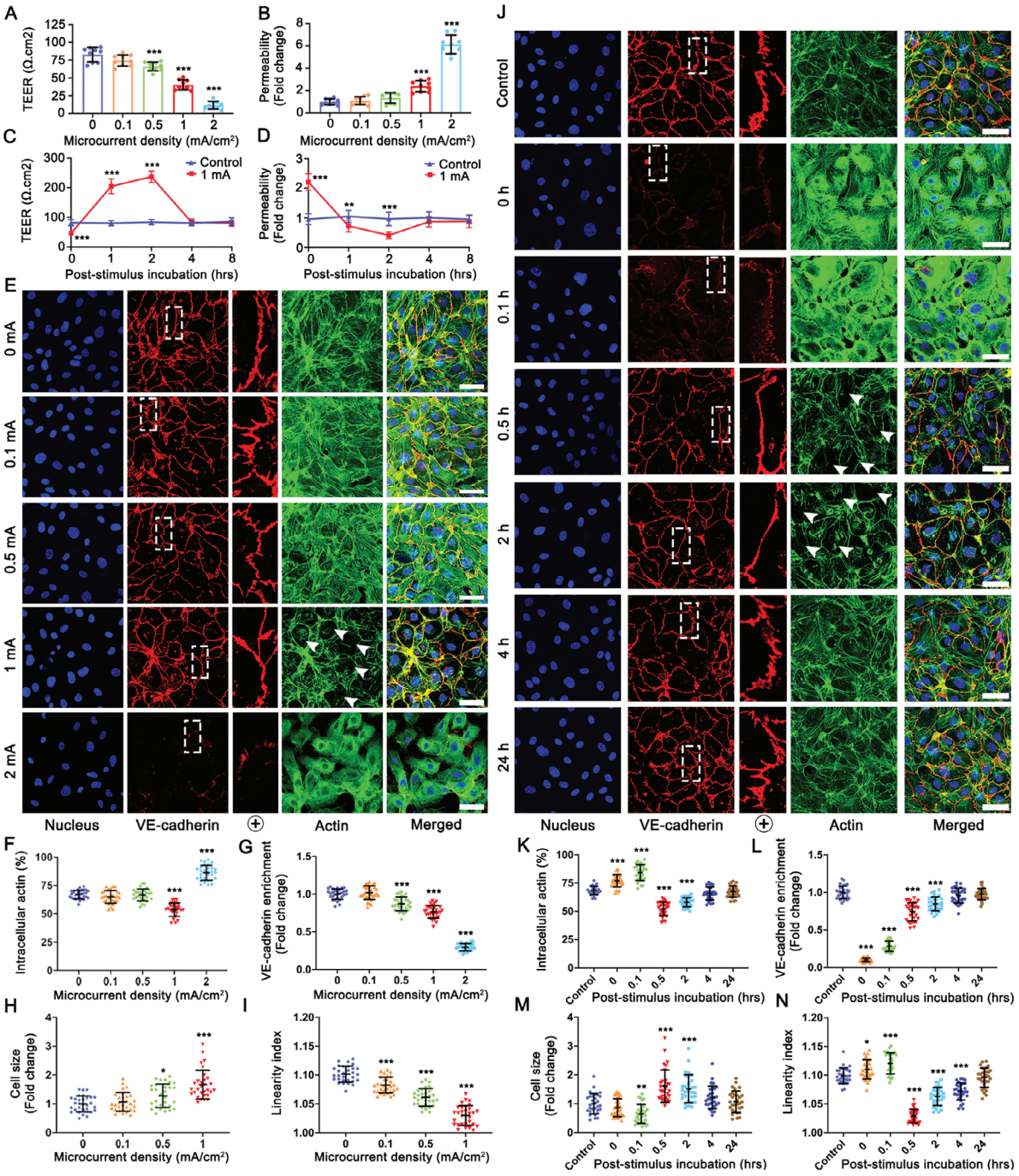

Figure 3. The endothelial permeability increased reversibly triggered by MDS in vitro. A,B) The transendothelial electrical resistance (TEER) and the permeability to 5 kDa FITC–dextran of HUVEC monolayers were measured following MDS exposure with different microcurrent densities. The data are presented as mean ± SD ($n = 9$). P values were analyzed by one-way ANOVA. C,D) The TEER and the permeability to 5 kDa FITC–dextran of HUVEC monolayers as function of post-exposure incubation time, for both control and MDS stimulated (7 min at 1 mA cm^{-2}). The data are presented as mean ± SD ($n = 9$). P values were analyzed by unpaired Student's *t*-test. E–I) Representative confocal microscopy images of HUVEC monolayers 0.5 h after MDS stimulation under varying microcurrent densities for 7 min. Scale bar, 50 µm. The middle column showing a magnification of the region indicated in the VE-cadherin channel. The white arrows point to the cytoplasm with reduced SFs. The percentage of intracellular actin (F), the relative VE-cadherin enriched in the junctional regions (G), the cell size (H) measured by the area enclosed by VE-cadherin, and the linearity index (I) defined as the ratio of the actual junction length to the linear junction length of VE-cadherin concerning that of untreated cells (Control). The data are presented as mean ± SD ($n = 30$). P values were analyzed by one-way ANOVA. J–N) Representative confocal microscopy images of HUVEC monolayers as function of incubation time after MDS stimulation at 1 mA cm^{-2} for 7 min. Scale bar, 50 µm. The middle column showing a magnification of the region indicated in the VE-cadherin channel. The white arrows point to the cytoplasm with reduced SFs. Scale bar, 50 µm. The intracellular actin (K), the VE-cadherin enrichment (L), the cell size (M), and the linearity index (N) are described above. The data are presented as mean ± SD ($n = 30$). P values were analyzed by one-way ANOVA. *p < 0.05, **p < 0.01, and ***p < 0.001.

permeation and piezo channel activation, which result in elevated intracellular Ca^{2+} levels.[17] Therefore, we focused on changes in intracellular Ca^{2+} levels caused by MDS. Intracellular Ca^{2+} levels increased immediately after MDS stimulation, followed by a rapid return to baseline within 0.5 h (**Figure** 4A). The influx of Ca^{2+} is known to activate the RhoA/ROCK pathway, leading to the formation of (SFs) and actomyosin contraction,[43] This process causes reversible invagination of VE-cadherin into the cell,[44] explaining the increase in intracellular SFs and the decrease in VE-cadherin fluorescence (Figure 3J) and insoluble VE-cadherin protein levels (Figure 4B,C) during the electro-stimulated phase (0–0.1 h). RhoA activity and ROCK protein levels increased significantly during the electro-stimulated phase (Figure 4D–F). Additionally, piezo channel inhibitor (ruthenium red), intracellular Ca^{2+} chelator (BAPTA-AM), and ROCK inhibitor (Y27632) all blocked the increase in intracellular SFs and the disappearance of VE-cadherin fluorescence during the electro-stimulated phase (Figure S8A, Supporting Information), further proving the key role of the Ca^{2+}-triggered RhoA/ROCK pathway in endothelial barrier leakage during the electro-stimulated phase.

During the electro-transformed phase (0.5–2 h), the fluorescence signal and protein level of VE-cadherin were restored, leading to a decrease in endothelial permeability, indicative of endothelial barrier stabilization. It is well established that cyclic adenosine monophosphate (cAMP) stabilizes endothelial barrier functions by regulating VE-cadherin.[45] We found that intracellular cAMP levels increased as Ca^{2+} levels decreased during the electro-stimulated phase and remained high during the electro-transformed phase (Figure 4G). The barrier-stabilizing effect of cAMP signaling is known to be mediated either by protein kinase A (PKA) or by exchange protein 1 activated by cAMP (EPAC1).[46] We observed a significant increase in PKA activity in electro-transformed cells (Figure 4H). Moreover, when cells were treated with PKA inhibitor (H-89) or EPAC1 inhibitor (ESI-09) before MDS stimulation, the linearization of VE-cadherin and the transformation of intracellular SFs to CBs were blocked by the former 0.5 h post-stimulation (Figure S8B, Supporting Information). cAMP signaling has been reported to activate PKA, which then inhibits actin contraction caused by RhoA/ROCK pathway activation.[47] Our results also demonstrated a significant down-regulation of RhoA activity and ROCK protein levels during the electro-transformed phase (Figure 4E,F).

Finally, we explored the interaction between Ca^{2+} and the second messenger cAMP signaling. We noted that the increase of intracellular cAMP after MDS stimulation was fairly insignificant in the absence of extracellular Ca^{2+} (Figure 4I). Furthermore, BAPTA-AM (BP), an intracellular Ca^{2+} chelator, was used to remove intracellular Ca^{2+}, and found that intracellular cAMP was significantly increased only in the presence of extracellular Ca^{2+} (Figure 4J), alluding to the strong dependence of the increase of cAMP on the influx of extracellular Ca^{2+} after MDS stimulation. Collectively, Ca^{2+}-dependent cAMP signaling pathway plays a pivotal role in the microcurrent-induced regulation of endothelial permeability. Figure 4K summarizes that the influx of Ca^{2+} activates the RhoA/ROCK axis during the electro-stimulated phase, leading to endothelial barrier leakage, and that subsequent Ca^{2+}-dependent cAMP signaling mediates PKA activation to stabilize the endothelial barrier by inhibiting the RhoA/ROCK axis during the electro-transformed phase.

2.5. MDS-Mediated PTH Efficient Delivery and Osteogenesis Enhanced In Vivo

To test the effect of microcurrent in MDS on PTH delivery efficiency, the PTH-preloaded MDS was inserted into a PBS solution. The preloaded PTH was delivered into the PBS solution through microchannels, driven by both the electric field and free diffusion (see Delivery Efficiency Test Section). The results showed that the microcurrent density was positively correlated with PTH delivery efficiency, and the delivery efficiency at 1 mA cm^{-2} was significantly higher than that achieved through free diffusion (control) (**Figure** 5A). Previous reports have also indicated that the driving force provided by microcurrent could increase drug permeation across the skin by 5–10 times compared to MNs alone.[48] The delivery efficiency of MDS was further verified in vivo by examining the plasma concentration profiles of PTH under different administration methods. Compared to the MMAs-PTH group (PTH delivered by MDS without microcurrent) and the SCI-PTH group, MDS delivery (1 mA cm^{-2} for 7 min) significantly reduced the plasma C_{max} time of PTH (Figure 5B). Previous studies proposed that the obstruction of subcutaneous capillary walls reduces the absorption rate of PTH post-SCI and causes approximately 20% subcutaneous residue, delaying the time to plasma C_{max} to 30 min followed by elimination in 4 h,[9] which is consistent with our results of SCI-PTH group. By providing an electro-driving force and reversibly increasing vascular permeability, MDS efficiently accelerates PTH entry into the blood, shortening the PTH exposure time to 2 h (Figure 5B).

To evaluate the osteoanabolic effect of PTH delivered by MDS, ovariectomized (OVX) OP rat models were established and subjected to different treatments: 1) SCI-PBS (sham and OVX); 2) MDS-PBS (MDS-delivered PBS in OVX); 3) SCI-PTH (PTH delivered via SCI in OVX); 4) MMAs-PTH (MDS-delivered PTH without microcurrent in OVX); 5) MDS-PTH (MDS-delivered PTH in OVX). PTH was administered at a concentration of 40 μg k^{-1}g once daily for one month. Micro-CT of the distal femurs revealed that the OVX and MDS-PBS groups experienced severe bone loss and destruction of bone microarchitecture compared to the sham group. The PTH-treated groups showed significant improvement in bone mass and bone microarchitecture compared to the OVX group, with the MDS-PTH group demonstrating an even greater increase in BMD and bone volume fraction (Figure 5C–H). Numerous studies have shown that direct current (DC) could promote osteogenic differentiation of mesenchymal stem cells and increase bone mass.[49,50] However, in these studies, the electrodes were directly applied to the bone, and the required current and voltage levels were significantly higher than the 1 mA cm^{-2} used in our MDS. Furthermore, there was no significant difference in bone mass between the MDS-PBS group and the OVX group, indirectly suggesting that localized transcutaneous microcurrent (1 mA cm^{-2}) has no substantial effect on bone-related cells (Figure 5C–H). Hematoxylin and eosin (H&E) staining and Masson's staining also exhibited marked trabecular microarchitecture deterioration in the OVX group, with new bone formation (indicated in blue) significantly promoted in the MDS-PTH group compared to the SCI-PTH group (Figure 5I,J). According to these findings, MDS enhanced osteogenic efficacy by reducing the PTH exposure time compared to conventional SCI.

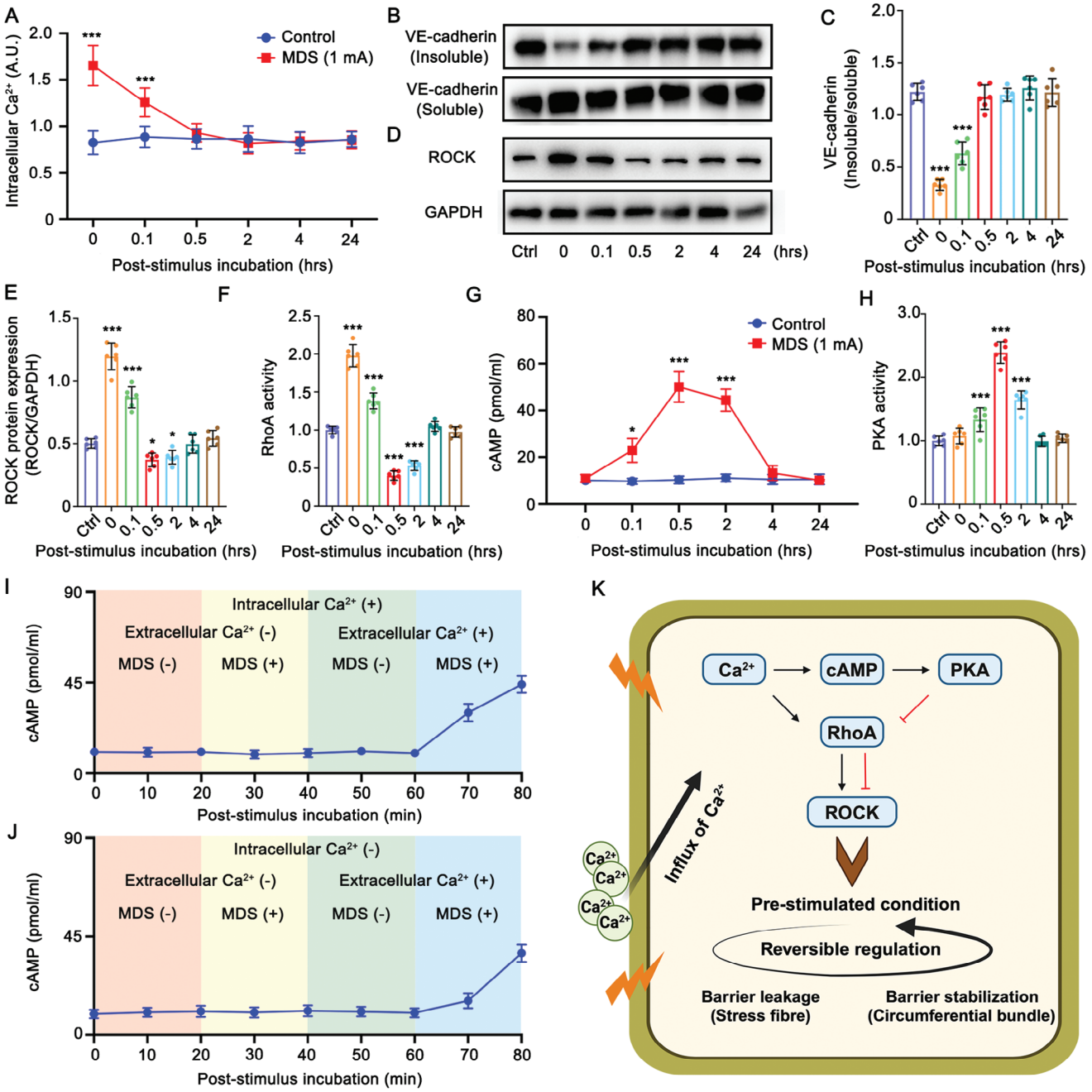

Figure 4. Ca^{2+}-dependent cAMP mediates reversible increase of endothelial permeability via ROCK activation and inhibition. A) Intracellular Ca^{2+} in HUVEC monolayers as function of post-stimulus time for both control (untreated) and MDS stimulation (1 mA cm^{-2} for 7 min) cells. The data are presented as mean ± SD (n = 3). P values were analyzed by unpaired Student's t-test. B–E) Western blot analyses of insoluble VE-cadherin, soluble VE-cadherin (total), ROCK and GAPDH protein samples in HUVEC monolayers triggered by MDS (1 mA cm^{-2} for 7 min) at different post-stimulus time (B,D). Quantitative analyses of insoluble VE-cadherin (C) and ROCK protein expression (E) relative to soluble VE-cadherin and GAPDH, respectively. Data are presented as mean ± SD (n = 6). P values were analyzed by one-way ANOVA. F) Relative RhoA activity in HUVEC monolayers triggered by MDS (1 mA cm^{-2} for 7 min) at different post-stimulus times with respect to that of control cells (untreated). Data are presented as mean ± SD (n = 6). P values were analyzed by one-way ANOVA. G) Intracellular cAMP levels in HUVEC monolayers as function of post-stimulus time for both control (untreated) and MDS stimulation (1 mA cm^{-2} for 7 min) cells. The data are presented as mean ± SD (n = 3). P values were analyzed by unpaired Student's t-test. H) Relative PKA activity in HUVEC monolayers triggered by MDS (7 min at 1 mA cm^{-2}) at different post-stimulus times with respect to that of control cells (untreated). Data are presented as mean ± SD (n = 6). P values were analyzed by one-way ANOVA. I, J) The effect of MDS stimulation (7 min at 1 mA cm^{-2}) and extracellular Ca^{2+} on intracellular cAMP levels in HUVEC monolayers with and without intracellular Ca^{2+}, respectively. Intracellular Ca^{2+} were chelated by BAPTA-AM. The data are presented as mean ± SD (n = 3). K) Mechanism diagram of spontaneous recovery of endothelial permeability. *p < 0.05 and ***p < 0.001.

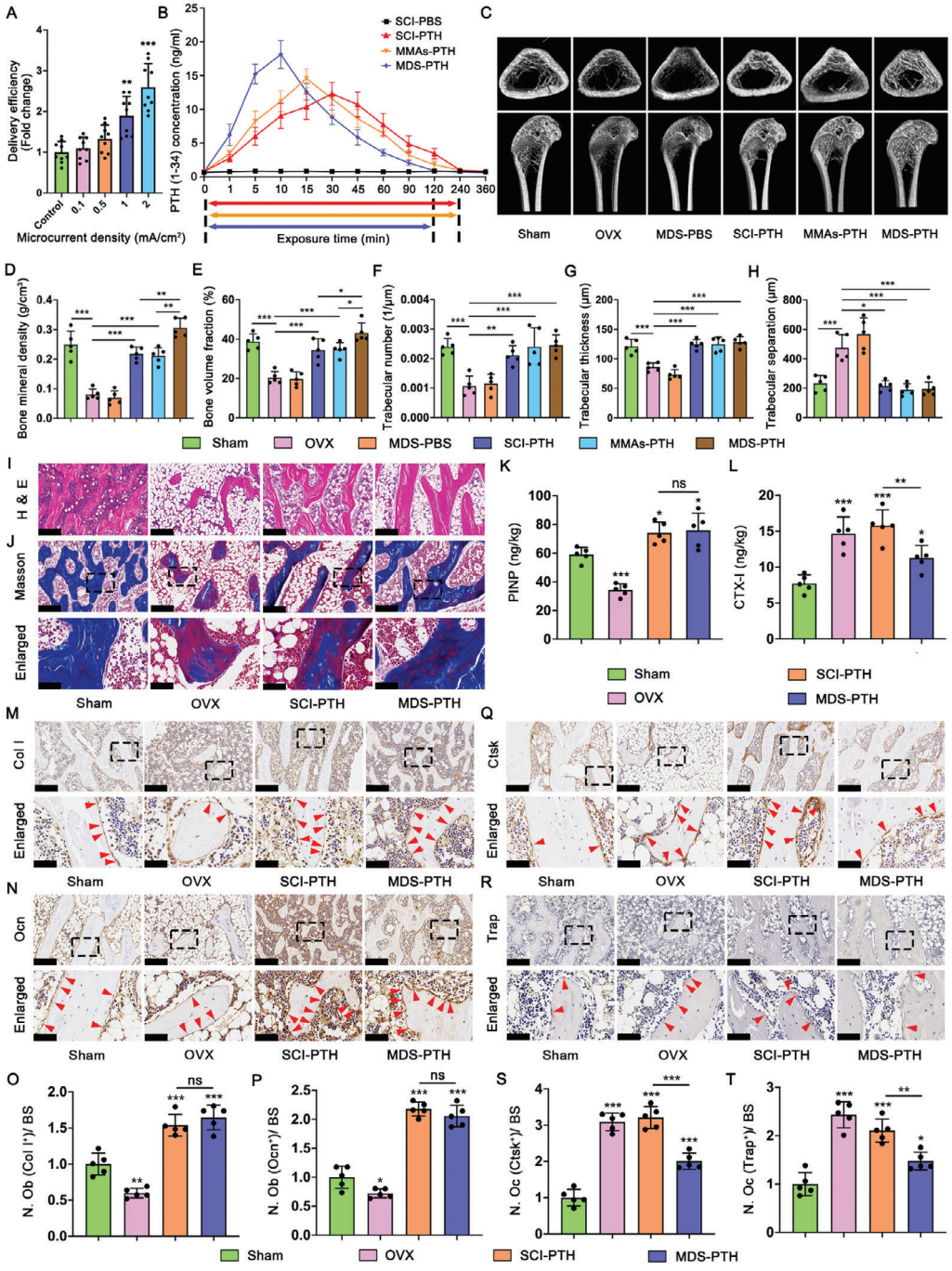

Figure 5. MDS-mediated PTH efficient delivery and osteogenic enhancement in vivo. A) PTH delivery efficiency of MDS at different microcurrent densities in vitro. Data are presented as mean ± SD ($n = 9$). P values were analyzed by one-way ANOVA. B) Plasma concentration-time profiles of PTH using three different delivery methods. Data are presented as mean ± SD ($n = 3$). C) 3D reconstruction of distal femurs from sham-operated and OVX rats treated with PBS or PTH by different methods for 4 weeks. D–H) Quantitative results of micro-CT: (D) bone mineral density, (E) bone volume fraction, (F) trabecular number, (G) trabecular thickness, and (H) trabecular separation. Data are presented as mean ± SD ($n = 5$). P values were analyzed by one-way ANOVA. I) Hematoxylin and eosin (H&E) staining of distal femurs. Scale bar, 200 μm. J) Masson staining of distal femurs from sham-operated and OVX rats. Blue marks new bone collagen fibers, while red marks mature bone. Scale bar, 200 μm. Enlarged scale bar, 50 μm. K,L) Plasma concentration of PINP and CTX-I. Data are presented as mean ± SD ($n = 5$). P values were analyzed by one-way ANOVA. M,N) Immunohistochemistry analyses for osteoblastic makers Col1 (M) and OCN (N). Col^+ and OCN^+ osteoblasts on the bone surface are marked by red arrows. Scale bar, 200 μm. Enlarged scale bar, 50 μm. O,P) The number of Col^+ and OCN^+ osteoblasts per bone surface. Data are presented as mean ± SD ($n = 5$). P values were analyzed by one-way ANOVA. Q) Immunohistochemistry analyses for osteoclastic makers Ctsk. $Ctsk^+$ osteoclasts on the bone surface are marked by red arrows. Scale bar, 200 μm. Enlarged scale bar, 50 μm. R) Trap staining for assessment of osteoclast activity. Red arrows indicate mature osteoclasts. Scale bar, 200 μm. Enlarged scale bar, 50 μm. S,T) The number of $Ctsk^+$ and $Trap^+$ osteoclasts per bone surface. Data are presented as mean ± SD ($n = 5$). P values were analyzed by one-way ANOVA. *p < 0.05, **p < 0.01, and ***p < 0.001.

The effect of MDS on reducing PTH exposure time and its impact on bone homeostasis was further analyzed. Serum enzyme-linked immunosorbent assay (ELISA) results indicated that the bone formation marker PINP increased notably in both the SCI-PTH and MDS-PTH groups compared to the OVX group, but there was no significant difference between the SCI-PTH and MDS-PTH groups. Although the bone resorption marker CTX-I was significantly increased in each group compared to the sham group, it was significantly lower in the MDS-PTH group than in the SCI-PTH group, suggesting that MDS-PTH enhanced the PTH osteoanabolic effect by inhibiting osteoclast metabolism (Figure 5K,L). Numerous studies have investigated the effect of PTH exposure time on bone turnover markers, concluding that prolonged exposure time via intravenous infusion leads to a significant increase in bone resorption markers.[7,8] Sections of distal femurs were further subjected to immunohistochemistry (IHC) staining for osteoblastic (Col/OCN) and osteoclastic markers (Ctsk/Trap). Compared with the OVX group, there were more Col^+ and OCN^+ osteoblasts per bone surface in the SCI-PTH and MDS-PTH groups, but no significant difference between the two (Figure 5M–P). However, there were dramatically fewer $Ctsk^+$ and $Trap^+$ osteoclasts per bone surface in the MDS-PTH group compared to the SCI-PTH group (Figure 5Q–T). Choi et al. found that a 30-min PTH exposure was sufficient to achieve maximal induction of the osteogenic gene Nurr1, while exposure for more than 2 h resulted in a sharp increase in the osteoclastic gene Rankl, peaking at 4 h at the transcriptional level.[6] To summarize, MDS reduced the PTH exposure time, attenuating osteoclast differentiation while ensuring osteoblast differentiation, ultimately enhancing the PTH osteoanabolic effect.

2.6. MDS for Safe Drug Delivery In Vivo

For the long-term daily administration of PTH, it is necessary to validate the biocompatibility of MDS in the skin and major organs. Histopathological analysis of skin biopsies showed negligible inflammation within 4 h after treatment with MDS, whether with or without microcurrent (MMAs), which was alleviated within 24 h (**Figure** 6A). After one month of PTH treatment, there was no significant difference in the appearance or weight of major organs in the MDS-PTH group compared to the SCI-PBS and SCI-PTH groups (Figure 6B,C). Finally, histopathological analysis showed no structural disruption in the visceral organs of the MDS-PTH group (Figure 6D). These results indicate the good biosafety of MDS for long-term delivery of PTH.

3. Conclusion

In this work, we developed an integrated and functional MDS to facilitate PTH delivery for an enhanced osteoanabolic effect. First, we elucidated the effect and mechanism of MDS in reversibly increasing vascular permeability in vitro. We then verified the high efficiency of MDS for PTH delivery both in vitro and in vivo, which resulted in a shorter PTH exposure time compared to SCI. Finally, OP rat models demonstrated that the enhanced osteoanabolic effect, due to the shortened PTH exposure time achieved by MDS, was accomplished by inhibiting osteoclast differentiation. The minimal invasiveness of MMAs makes them advantageous for preventing vascular and nerve damage, penetrating skin tissue, and delivering drugs in situ, making them applicable in a wide range of scenarios, including transdermal drug delivery. The built-in microchannels of MMAs provide a concentrated electric field for MDS, which not only accelerates the movement of subcutaneous drugs but also facilitates circulatory absorption by increasing vascular permeability reversibly. As a general localized subcutaneous drug delivery platform, MDS may serve as a more versatile tool, broadly applicable to macromolecular drugs in addition to PTH. Additionally, MDS allows for self-administration due to its safety and user-friendliness, offering high practicality.

4. Experimental Section

Fabrication and Characterization of MDS: The MMAs were printed by a high-resolution 3D printer (Miro P213, Xingsheng Technology Inc., Jiangmen, China) with an accuracy of 3 µm, using XS-BIO resin (35% polyester acrylate, 25% glycidyl methacrylate, 25% poly (ethylene glycol) dimethacrylate and 15% Polyethylene glycol; Xingsheng Technology Inc., Jiangmen, China) and was cured under 405 nm UV light. Software SolidWorks 2022 was applied to design the 3D model of the MMAs, and then the model was sliced into a series of 2D images (5 µm per slice). Figure S2 (Supporting Information) shows representative printing layers and corresponding projecting images of MMAs. Similarly, the injection cap matching the size of MMAs was designed and printed, with the diameter of the circular groove for loading MMAs being 8 mm, and the diameter of the drug reservoir being 5 mm.

The positive electrode was constructed using the pusher head of the syringe: flatten the rubber pusher head with a blade, and then sputter a layer of silver onto the flat surface. The silver wire connecting the power supply was fixed by the silver paste on the sputtered silver electrode. The tip of the syringe can be inserted into the injection cap for application.

As the negative electrode, counter electrode MNs were fabricated by laser microetching (Inno Laser Technology Co., Ltd, Shenzhen, China) using a stainless steel substrate with a thickness of about 100 µm. An Au layer of about 100 nm thickness was coated on the surface of the counter electrode MNs to enhance biocompatibility using magnetron sputtering (Kangdesheng Mechanical & Electrical Technology Co., Ltd., China), and the counter electrode MNs were then inserted into the corresponding slot of the injection cap to construct the MDS.

Above morphologies were characterized by an optical microscope (Axio Zoom V16, Zeiss) and scanning electron microscope (SEM, SUPRA 60, Zeiss).

Mechanical Properties of MMAs: A low-force mechanical testing system (GCD-203050 M, Daheng Optics, Beijing) was applied to test the mechanical properties of the MMAs. Briefly, the needle tips of MMAs pointed up and a compressive load was applied with increasing force up to the maximum loading force of 40 N. The time sensitivity of the compressive sensor probe is 0.1 s. For the deformation test, 20 N compressive force was maintained for 20 s in each group before MMAs were taken out for observation under an SEM.

Skin Penetration Test: The needle tips of MMAs were stained with red fluorescent dye using a porous sponge filled with rhodamine B (Sigma Aldrich, Merck). The MMAs were pressed into a piece of porcine skin and removed 5 min later. The position on the porcine skin treated by MMAs was cut into a 2 cm slice, then using the fluorescence microscope (IX83, Olympus) to record the penetration effect of the cross-section.

Cell Culture: HUVECs were cultured in endothelial cell medium (ECM, ScienCell) containing 5% FBS, 1% endothelial cell growth factor supplement, and 1% antibiotic and were maintained at 37 °C in a humidified atmosphere containing 5% CO_2. After 80–90% confluency, cells can be detached by 0.05% trypsin–EDTA and reseeded for passages. Cells between 4 and 6 passages were used in all experiments.

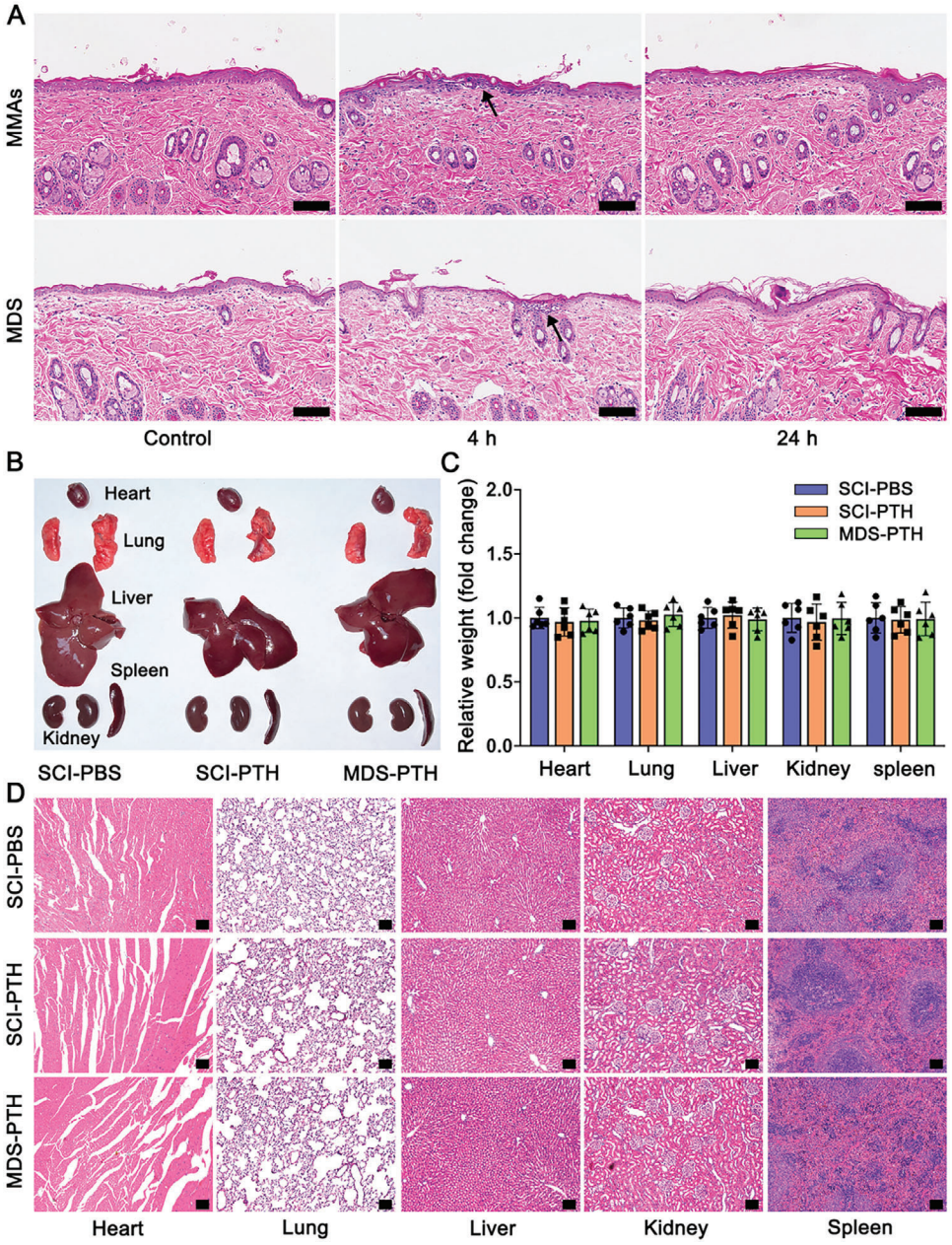

Figure 6. MDS for safe PTH delivery in vivo. A) Representative images of skin from the back of hairless rats after the treatment of MMAs (MDS without microcurrent) or MDS (1 mA cm^{-2}) for 7 min. Compared to the untreated sites (control), the H & E staining showed more scattered immune cells (black arrows) at 4 h after treatments, which alleviated within 24 h. Scale bar, 100 µm. B) Representative photographs of the heart, lung, liver, kidney, and spleen at the end of the experiment. C) Statistical analysis of the final weight of organs. Data are presented as mean ± SD ($n = 3$). P values were analyzed by one-way ANOVA. D) H&E staining of the heart, lung, liver, kidney, and spleen of rats at the end of the experiment. Scale bar, 100 µm.

Measurement of TEER: The integrity of endothelial barrier was assessed by the TEER across the HUVEC monolayer. HUVECs were seeded on polycarbonate membrane inserts of a 24-well Transwell (Corning, USA) coated with 0.1% gelatin at a density of 3×10^5 cells/insert and cultured for 2 days until HUVEC monolayer formation. The Millicell ERS-2 Electrical Resistance System (Millipore, USA) was applied to measure the TEER values. The normalized value was corrected for the background TEER of a filter without cells and expressed as Ω. cm^2 based on the corresponding surface area of filter.

Endothelial Permeability Assay: The HUVEC monolayer was formed on inserts of a 24-well transwell using the method described above. The endothelial permeability of the HUVEC monolayer was determined by the flux per unit time of FITC-dextran (M.W. 5 kDa) from the upper to the lower compartments of the Transwell. Briefly, 20 µM FITC-dextran was added to the upper compartment, and the same amount of unlabeled dextran was added to the lower compartment to balance the osmotic pressure. Then, the HUVEC monolayer was exposed to MDS according to the designed protocol. 10 µl of each sample was collected from both compartments at

various post-exposure incubation times. Fluorescence intensities of FITC-dextran (485 ex/520 em nm) were assessed using a microplate reader (Thermo Scientific, Varioskan LUX, USA). The amount of FITC–dextran transported to the lower compartment can be calculated by the standard curve.

Immunofluorescence and Analysis: HUVEC monolayers were fixed with 4% paraformaldehyde for 10 min at 4 °C. The fixed cells were permeabilized with 0.1% Triton-X for 5 min and blocked with 3% BSA in PBS for 1 h. The primary antibody (anti-VE-cadherin, 1:400, CST 2500, USA) was incubated at 4 °C overnight, and the secondary antibody (anti-rabbit, 1:1000, Alexa Fluor 647 Conjugate, CST, USA) was incubated at room temperature for 1 h. Actin filaments were stained with phalloidin (iFluor 488 Conjugate, 1:1000, AAT Bioquest, USA) and the nuclei were counterstained with DAPI (Beyotime, 1:500, Shanghai, China). PBS was used to wash thrice between each step. Fluorescence images were recorded by confocal microscopy (FV3000, Olympus), and all images were acquired under the same acquisition parameters.

Image J was used for the evaluation of immunofluorescence images. Briefly, The VE-cadherin enrichment was measured by the mean fluorescence intensity of VE-cadherin (red) at the intercellular junction of the maximum intensity projected image. The intracellular actin was evaluated using a masking approach, which eliminated the actin covered by VE-cadherin at the intercellular junction in the merged image. Cell sizes (area) were defined by their VE-cadherin structure. The linearity index was defined as the ratio of the actual junction length to the linear junction length of VE-cadherin.

Intracellular Ca^{2+}: The level of free cytoplasmic Ca^{2+} in HUVEC monolayers were determined by Fura-2 AM Ca^{2+} fluorescence probe. Briefly, the HUVEC monolayers were incubated in 5 μmol L^{-1} Fura-2 AM in PBS at 37 °C in the dark for 40 min. Then extracellular Fura-2 AM was removed by PBS change, and the measurements were carried out after another 20 min incubation period. The fluorescence intensity at 510 nm emission wavelength with excitation wavelengths of 340 nm and 380 nm were measured respectively by a microplate reader. The ratio of fluorescence intensity at 340 nm to 380 nm (340/380) represents the concentration of intracellular Ca^{2+}.

Intracellular cAMP: For cAMP assay, HUVEC monolayers were grown in 24-well plates treated with 100 μM IBMX (phosphodiesterase inhibitor) to prevent the hydrolysis of cAMP. HUVEC monolayers were exposed to the MDS followed by incubation at different time points. Then cells were lysed by repeated freeze/thaw, and the supernatant was supplied with the cAMP Parameter Immunoassay Kit (KGE002B, R&D Systems, Minneapolis, USA) according to the manufacturer's instructions.

Western Blotting: RIPA was used to extract proteins from lysed cells, and the proteins were then transferred to nitrocellulose membranes separated by SDS-PAGE electrophoresis. The membranes were blocked for 1 h using 5% skim milk followed by being incubated with primary antibodies (anti-VE-cadherin, 1:1000, CST 2500; anti-ROCK, 1:5000, Abcam ab45171) overnight at 4 °C and then with appropriate secondary antibodies (anti-rabbit IgG, 1:2000, CST 7074) for 1 h at room temperature. GAPDH was used as the housekeeping gene. Protein bands were visualized using a multifunctional imager (Amersham Imager 600, GE Healthcare, USA). Image J software was used for photo analysis.

Measurement of Soluble and Insoluble VE-Cadherin: The cell lysate was isolated from the cytoskeleton extraction buffer[51] via centrifugation at 12000 × g for 10 min. The cytoskeleton-associated insoluble fraction in the pellet was then incubated at 100 °C for 10 min. Both the cytoskeleton-associated insoluble and soluble (soluble) fractions were quantified by BCA assay. SDS-PAGE and western blotting were applied to isolate and analyze, respectively.

Inhibitor Assay: The inhibitors were used as follows. ROCK inhibitor (Y-27632, MCE HY-10071): 15 μM; intracellular Ca^{2+} chelator (BAPTA-AM, MCE HY-100545): 20 μM; piezo channel inhibitor (ruthenium red, MCE HY-103311): 20 μM; Epac1 inhibitor (ESI-09, MCE HY-16704): 10 μM; PKA inhibitor (H-89, MCE HY-15979): 10 μM.

Elisa (PINP, CTX-I and PKA) and Glisa (RhoA): Elisa kits were used to detect the expression of PINP (Huamei, Wuhan, China) and CTX-I (Meilian, Shanghai, China). Plasma samples from different groups were obtained by the rat facial veins and then separated by centrifuging at 1000 g for 30 min at 4 °C. PKA Colorimetric Activity Kit (Arbor Assays, Ann Arbor, USA) was used to evaluate the activity of PKA. The HUVEC monolayers at different time points after MDS treatment (1 mA cm^{-2} for 7 min) were lysed in the activated cell lysis buffer provided by the kit, and the supernatant was separated for subsequent detection. According to the manufacturer's protocols, the related reagents were added to wells of Elisa plates according to the instructions and incubated at 37 °C. Following the termination of the reaction, the optical densities of the wells were recorded by a microplate reader, and the relative concentrations were calculated.

The RhoA Glisa kit (Cytoskeleton, Denver CO, USA) was used to evaluate RhoA activity according to manufacturer's recommendations. Briefly, cell lysates were harvested at 4 °C and then added to the wells of the RhoA binding plates after adjusting the protein concentration. Plates were incubated at 4 °C for 1 h and then washed twice with wash buffer at room temperature. RhoA primary antibodies (1:200) were added and incubated for 1 h at room temperature. Following the HRP-related antibody and detection reagent were added, the results were analyzed using a microplate reader.

Delivery Efficiency Test: All microchannels of the MMAs preloaded with the PTH solution using the syringe push rod, and then the MDS and the counter electrode MNs were placed into PBS solution. The power supply (HLR-3660D, Guangdong Henghuiyuan Electronics Co., Ltd, China) was turned on to deliver different microcurrent densities for 5 min. The control group was treated in the same manner but no power supply. The PBS solution from each group was collected and their concentration of PTH was determined by Elisa kit (High Sensitivity Human PTH EIA, Quidel MicroVue, USA) according to manufacturer's recommendations. Delivery efficiency was defined as the concentration of PTH in PBS per unit of time.

Pharmacokinetics of PTH: The abdominal skin of Sprague Dawley rats was shaved while the animals were anesthetized by pentobarbital sodium salt (30 mg $k^{-1}g$). Twelve rats (12 weeks old, female) were randomly divided into four groups: 1) SCI-PBS: SCI with 200 μl PBS; 2) SCI-PTH: SCI with 200 μl PTH (40 μg $k^{-1}g$); 3) MMAs-PTH: 200 μl PTH (40 μg $k^{-1}g$) subcutaneously delivered by MDS using the syringe push rod without microcurrent; 4) MDS-PTH: 200 μl PTH (40 μg $k^{-1}g$) was first subcutaneously delivered by MDS using the syringe push rod and then 1 mA cm^{-2} of microcurrent was applied for 7 min. At pre-determined intervals (1, 5, 10, 15, 30, 45, 60, 90, 120, 240, 360 min), 100 μl of blood was withdrawn from the jugular veins and collected in tubes containing EDTA. The plasma was separated from the collected blood and then stored at −80 °C until required for determination of PTH concentration. The PTH Elisa kit was used to evaluate PTH concentration (see Delivery Efficiency Test Section). The time to reach peak PTH plasma concentration (T_{max}) was determined directly from the plasma concentration-time profiles.

Animal Model Grouping and Treatment: All rats used in this study were obtained from the Animal Experimental Center of Sun Yat-sen University, and all procedures were approved by the Committee on the Ethics of Animal Experiment Center of Sun Yat-sen University (Approval No. SYSU-IACUC-2024-B0801). Thirty Sprague–Dawley rats (12 weeks old, female) were used to establish the postmenopausal OP model. All animals were anesthetized by pentobarbital sodium salt (30 mg $k^{-1}g$). Under sterile conditions, the bilateral ovaries were exposed through dorsal midline incision and removed in the ovariectomy group (OVX, 25 rats), whereas only two pieces of adipose tissues with volumes equivalent to those of the ovaries were removed in the sham group (5 rats). The bilateral oophorectomy was confirmed to be successful when pap smear screening showed no keratosis. Three months after surgery, rats of the OVX group were randomly divided into five treatment groups: 1) OVX (SCI with PBS); 2) MDS-PBS (PBS delivered by MDS (1 mA cm^{-2} for 7 min)); 3) SCI-PTH (SCI with PTH (40 μg $k^{-1}g$)); 4) MMAs-PTH: PTH (40 μg $k^{-1}g$) was subcutaneously delivered by MDS using the syringe push rod without microcurrent; 5) MDS-PTH: PTH (40 μg $k^{-1}g$) was first delivered subcutaneously by MDS using the syringe push rod, followed by the application of a 1 mA cm^{-2} microcurrent for 7 min. The sham group was injected subcutaneously with PBS. All treatments were performed once a day for one month.

Micro-CT Evaluation: The BMD and trabecular bone parameters of rats were detected after one month of treatments. The anesthetized rats

were subjected to micro-CT examination using a SkyScan 1276 benchtop scanner (Bruker, Kontich, Belgium). The left femurs were analyzed, and the trabecular region of interest (ROI) was located 0.5 mm above the growth plate and extended 1.5 mm upward. All left femurs were scanned at an isotropic voxel resolution of 20 µm with a 0.5 mm aluminum filter, 70 kV x-ray tube voltage, 200 µA tube electric current, and 460 ms exposure time. The BMD and the trabecular bone parameters were quantitatively analyzed by software CTAn (Version 1.17.7.2, SkyScan). According to the ROI, the locational trabecular bone was reconstructed at 3D levels using the software CTvox (Version 3.2, Skyscan).

Histological Evaluation: The excised skin, visceral tissue and femurs were dissected and fixed in 4% paraformaldehyde for 48 h at room temperature. The femurs needed to be decalcified for three weeks. All tissues were embedded in paraffin and sectioned continuously (5 mm thick). H&E and Masson staining were performed according to previous protocol.[52] For tartrate-resistant acid phosphatase (TRAP) staining, the TRAP staining kit (SLBT1113, Sigma, USA) was applied according to the manufacturer's instructions. Immunohistochemistry staining was performed according to previous protocols.[53] The following primary antibodies were used: anti-Col1 (Collagen I, Abcam ab270993, 1:100), anti-Ocn (Osteocalcin, Boster PB1009, 1:200), anti-Ctsk (cathepsin K, Santa Cruz sc-48353, 1:50). The slides were photographed using a microscope (IX83, Olympus). The number of positive cells per unit bone surface was quantified by Image J.

Statistical Analysis: Statistical analyses were performed using GraphPad Prism 10 software. Data presented in this study are expressed as the mean ± SD. A minimum of three replicates were used in each process for all experiments. The data was analyzed using ordinary one-way analysis of variance (ANOVA) or unpaired Student's *t*-test. P-values below 0.05 (*$p < 0.05$, **$p < 0.01$, and ***$p < 0.001$) were considered significant differences between groups.

Supporting Information

Supporting Information is available from the Wiley Online Library or from the author.

Acknowledgements

X.M. and K.M. These authors contributed equally to this work. The authors would like to acknowledge financial support from the National Natural Science Foundation of China (Grant No. 32171456, 82272527, 82072520), Guangdong Basic and Applied Basic Research Foundation (Grant No. 2023A1515111003), the China Postdoctoral Science Foundation (Grant No. 2024M751327), the President Foundation of Nanfang Hospital, Southern Medical University (Grant No. 2023B020). Additionally, the authors thank Material Scientific Cores at Zhejiang Lab for the assistance.

Conflict of Interest

The authors declare no conflict of interest.

Data Availability Statement

The data that support the findings of this study are available from the corresponding author upon reasonable request.

Keywords

microchannels, microcurrent, microneedle, osteoanabolic effect, PTH

Received: July 24, 2024
Revised: October 8, 2024
Published online: October 17, 2024

[1] X. Mo, S. Zhao, Z. Wen, W. Lin, Z. Chen, Z. Wang, C. Huang, J. Qin, J. Hao, B. Chen, *BMC Geriatr.* **2021**, *21*, 361.
[2] F. Cosman, *Endocr. Pract.* **2020**, *26*, 777.
[3] L. Osagie-Clouard, A. Sanghani, M. Coathup, T. Briggs, M. Bostrom, G. Blunn, *Bone Joint Res.* **2017**, *6*, 14.
[4] Y. He, M. Li, G. Tong, Y. Meng, S. Hao, S. Hu, W. Yan, D. Yang, *Bone* **2020**, *135*, 115326.
[5] C. A. Frolik, E. C. Black, R. L. Cain, J. H. Satterwhite, P. L. Brown-Augsburger, M. Sato, J. M. Hock, *Bone* **2003**, *33*, 372.
[6] H. Choi, C. E. Magyar, J. M. Nervina, S. Tetradis, *PLoS One* **2018**, *13*, 0208514.
[7] H. Dobnig, R. T. Turner, *Endocrinology* **1997**, *138*, 4607.
[8] M. Shimizu, H. Noda, E. Joyashiki, C. Nakagawa, K. Asanuma, A. Hayasaka, M. Kato, M. Nanami, M. Inada, C. Miyaura, T. Tamura, *Biol. Pharm. Bull.* **2016**, *39*, 625.
[9] P. E. Daddona, J. A. Matriano, J. Mandema, Y. F. Maa, *Pharm. Res.* **2011**, *28*, 159.
[10] M. Dang, A. J. Koh, T. Danciu, L. K. McCauley, P. X. Ma, *Adv. Healthcare Mater.* **2017**, *6*, 1600901.
[11] Y. Nabuchi, E. Fujiwara, H. Kuboniwa, Y. Asoh, H. Ushio, *Pharm. Res.* **1997**, *14*, 1685.
[12] B. Markelc, E. Bellard, G. Sersa, T. Jesenko, S. Pelofy, J. Teissie, R. Frangez, M. P. Rols, M. Cemazar, M. Golzio, *J. Control Release* **2018**, *276*, 30.
[13] P. Mohana Sundaram, K. K. Rangharajan, E. Akbari, T. J. Hadick, J. W. Song, S. Prakash, *Lab Chip* **2021**, *21*, 319.
[14] N. Rahimi, *Front Immunol.* **2017**, *8*, 1847.
[15] A. Abu Taha, H. J. Schnittler, *Cell Adh. Migr.* **2014**, *8*, 125.
[16] L. Li, J. Xin, H. Wang, Y. Wang, W. Peng, N. Sun, H. Huang, Y. Zhou, X. Liu, Y. Lin, J. Fang, B. Jing, K. Pan, Y. Zeng, D. Zeng, X. Qin, Y. Bai, X. Ni, *Ecotoxicol. Environ. Saf.* **2023**, *257*, 114940.
[17] P. M. Graybill, R. V. Davalos, *Cancers* **2020**, *12*, 1132.
[18] L. M. Cancel, K. Arias, M. Bikson, J. M. Tarbell, *Sci. Rep.* **2018**, *8*, 9265.
[19] C. Beaudart, S. Silverman, D. T. Gold, S. A. Williams, R. Weiss, M. Hiligsmann, *Arch. Osteoporos.* **2022**, *17*, 57.
[20] Y. Suzuki, Y. Nagase, K. Iga, M. Kawase, M. Oka, S. Yanai, Y. Matsumoto, S. Nakagawa, T. Fukuda, H. Adachi, N. Higo, Y. Ogawa, *J. Pharm. Sci.* **2002**, *91*, 350.
[21] B. M. Medi, J. Singh, *Int. J. Pharm.* **2003**, *263*, 25.
[22] X. Jiang, H. Wu, A. Xiao, Y. Huang, X. Yu, L. Chang, *Small Methods* **2024**, *8*, 2301068.
[23] Y. Li, J. Yang, Y. Zheng, R. Ye, B. Liu, Y. Huang, W. Zhou, L. Jiang, *Acta Biomater.* **2021**, *121*, 349.
[24] U. Detamornrat, M. Parrilla, J. Dominguez-Robles, Q. K. Anjani, E. Larraneta, K. De Wael, R. F. Donnelly, *Lab Chip* **2023**, *23*, 2304.
[25] Y. Yang, L. Xu, D. Jiang, B. Z. Chen, R. Luo, Z. Liu, X. Qu, C. Wang, Y. Shan, Y. Cui, H. Zheng, Z. Wang, Z. L. Wang, X. D. Guo, Z. Li, *Adv. Funct. Mater.* **2021**, *31*, 2104092.
[26] M. Parrilla, U. Detamornrat, J. Dominguez-Robles, S. Tunca, R. F. Donnelly, K. De Wael, *ACS Sens.* **2023**, *8*, 4161.
[27] S. Choo, S. Jin, J. Jung, *Pharmaceutics* **2022**, *14*, 766.
[28] X. Li, X. Huang, J. Mo, H. Wang, Q. Huang, C. Yang, T. Zhang, H. J. Chen, T. Hang, F. Liu, L. Jiang, Q. Wu, H. Li, N. Hu, X. Xie, *Adv. Sci.* **2021**, *8*, 2100827.
[29] X. Y. Mo, Z. X. Wen, S. L. Zhao, J. S. Mo, F. M. Liu, M. W. Chen, C. Y. Zhan, M. Zhang, J. Wang, S. F. Wen, X. Xie, H. J. Chen, B. L. Chen, *Mater. Des.* **2022**, *219*, 14.
[30] I. Xenikakis, K. Tsongas, E. K. Tzimtzimis, O. L. Katsamenis, E. Demiri, C. K. Zacharis, D. Georgiou, E. P. Kalogianni, D. Tzetzis, D. G. Fatouros, *J. Drug Deliv. Sci. Technol.* **2022**, *67*, 14.
[31] H. Chang, S. W. T. Chew, M. Zheng, D. C. S. Lio, C. Wiraja, Y. Mei, X. Ning, M. Cui, A. Than, P. Shi, D. Wang, K. Pu, P. Chen, H. Liu, C. Xu, *Nat. Biomed. Eng.* **2021**, *5*, 1008.

[32] Y. W. Ding, Y. Li, Z. W. Zhang, J. W. Dao, D. X. Wei, *Bioact. Mater.* **2024**, *38*, 95.
[33] S. P. Davis, B. J. Landis, Z. H. Adams, M. G. Allen, M. R. Prausnitz, *J. Biomech.* **2004**, *37*, 1155.
[34] N. R. Rajagopalan, W. R. Vista, M. Fujimori, L. Vroomen, J. M. Jimenez, N. Khadka, M. Bikson, G. Srimathveeravalli, *Ann. Biomed. Eng.* **2024**, *52*, 89.
[35] S. N. Rampersad, J. D. Ovens, E. Huston, M. B. Umana, L. S. Wilson, S. J. Netherton, M. J. Lynch, G. S. Baillie, M. D. Houslay, D. H. Maurice, *J. Biol. Chem.* **2010**, *285*, 33614.
[36] W. H. Parker, E. M. Rhea, Z. C. Qu, M. R. Hecker, J. M. May, *Am. J. Physiol. Cell Physiol.* **2016**, *311*, C652.
[37] C. Anastasio, I. Donisi, A. Colloca, N. D'Onofrio, M. L. Balestrieri, *Int. J. Mol. Sci.* **2024**, *25*, 5087.
[38] H. Zhao, P. Wang, X. Wang, W. Du, H. H. Yang, Y. Liu, S. N. Cui, W. Huang, T. Peng, J. Chen, C. Gao, Y. Wang, S. Sadayappan, C. Ma, Y. Fan, C. Wang, G. C. Fan, *Cardiovasc. Res.* **2023**, *119*, 1981.
[39] L. Lin, Y. Wang, M. Cai, X. Jiang, Y. Hu, Z. Dong, D. Yin, Y. Liu, S. Yang, Z. Liu, J. Zhuang, Y. Xu, C. F. Guo, L. Chang, *Adv. Funct. Mater.* **2022**, *32*, 2109187.
[40] C. J. Meulenberg, V. Todorovic, M. Cemazar, *PLoS One* **2012**, *7*, e52713.
[41] J. Yang, Y. Li, R. Ye, Y. Zheng, X. Li, Y. Chen, X. Xie, L. Jiang, *Microsyst. Nanoeng.* **2020**, *6*, 112.
[42] M. G. Lampugnani, M. Resnati, M. Raiteri, R. Pigott, A. Pisacane, G. Houen, L. P. Ruco, E. Dejana, *J. Cell Biol.* **1992**, *118*, 1511.
[43] D. Kugelmann, L. T. Rotkopf, M. Y. Radeva, A. Garcia-Ponce, E. Walter, J. Waschke, *Sci. Rep.* **2018**, *8*, 13229.
[44] H. Geyer, R. Geyer, M. Odenthal-Schnittler, H. J. Schnittler, *Glycobiology* **1999**, *9*, 915.
[45] Y. Baumer, D. Drenckhahn, J. Waschke, *Histochem. Cell Biol.* **2008**, *129*, 765.
[46] H. Chen, Y. Shen, Y. Liang, Y. Qiu, M. Xu, C. Li, *Biol. Pharm. Bull.* **2022**, *45*, 1043.
[47] L. Li, Y. Yang, H. Zhang, Y. Du, X. Jiao, H. Yu, Y. Wang, Q. Lv, F. Li, Q. Sun, Y. Qin, *Front. Pharmacol.* **2021**, *12*, 723922.
[48] N. Khare, P. Shende, *Drug Dev. Ind. Pharm.* **2021**, *47*, 1183.
[49] J. Sun, W. Xie, Y. Wu, Z. Li, Y. Li, *Adv. Sci.* **2024**, 2404190.
[50] B. Yu, Z. Qiao, J. Cui, M. Lian, Y. Han, X. Zhang, W. Wang, X. Yu, H. Yu, X. Wang, K. Lin, *Biomaterials* **2021**, *276*, 120997.
[51] T. J. Wright, L. Leach, P. E. Shaw, P. Jones, *Exp. Cell Res.* **2002**, *280*, 159.
[52] C. Yu, W. Yang, L. Yang, L. Ye, R. Sun, T. Gu, X. Ying, M. Wang, R. Tang, S. Fan, S. Yao, *ACS Appl. Mater. Interfaces* **2023**, *15*, 19976.
[53] X. Han, F. Wang, J. Shen, S. Chen, P. Xiao, Y. Zhu, W. Yi, Z. Zhao, Z. Cai, W. Cui, D. Bai, *Adv. Mater.* **2024**, *36*, 2306993.

